ACS APPLIED MATERIALS & INTERFACES

www.acsami.org

Research Article

Synthesis of Self-Assembled Single Atomic Layer Gold Crystals-Goldene

Sudhir Kumar Sharma, Renu Pasricha, James Weston, Thomas Blanton, and Ramesh Jagannathan*

Cite This: *ACS Appl. Mater. Interfaces* 2022, 14, 54992−55003

Read Online

ACCESS | Metrics & More | Article Recommendations | Supporting Information

ABSTRACT: We report, for the first time, a technique to synthesize free-standing, one-atom thick 2D gold crystals (namely, goldene) and self-assembled 2D periodic arrays of goldene. High-resolution transmission electron microscopy (HRTEM) imaging of goldene revealed herringbone and honeycomb lattices, which are primarily gold surface features due to its reconstruction. Imaging of these surface-only features by a nonsurface characterization technique such as HRTEM is an unequivocal proof of the absence of three-dimensionality in goldene. Atomic force microscopy confirmed 1−2 Å thickness of goldene. High-resolution X-ray photoelectron spectroscopy (HR-XPS), selective area electron diffraction, and energy-dispersive X-ray spectroscopy confirmed the chemical identity of goldene. We discovered the phenomenon of electric field-induced self-assembly of goldene supracrystals with a herringbone structure and developed an electric field printing (e-print) technique for goldene arrays. Goldene showed a semiconductor response with a knee voltage of ∼3.2 V, and I/V spectroscopy revealed periodic room temperature Coulomb blockade oscillations. These observations are consistent with the theoretical calculations reported in the literature predicting enhanced Coulombic interactions between gold valence electrons and the nucleus in stable 2D gold. Goldene exhibited multiple, intense, and well-resolved optical absorption peaks and several fine bands across the UV−vis region, and we calculated its optical band gap to be 3.59 eV. Magnetic force microscopy measurements of goldene periodic arrays showed a ∼5 mV peak amplitude confirming its ferromagnetism. Optical and magnetic properties of goldene are consistent with those reported in the literature for 2D planar gold clusters with less than 12 atoms.

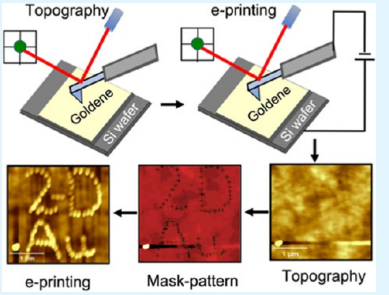

KEYWORDS: *2D materials, one-atom thick gold, goldene, self-assembly, atomic force microscopy, high resolution-X-ray photoelectron spectroscopy, transmission electron microscopy, magnetic force microscopy*

INTRODUCTION

Two-dimensional (2D) materials, which are single crystalline layer of atoms or molecules, are of significant interest to researchers because of their applications across varied disciplines.[1−4] Advances in 2D materials have led to significant research activities in the so-called field of van der Waals (vdW) crystals and spintronics with an emphasis on the discovery of a room-temperature vdW ferromagnetic spin source.[5−8] Recent advances in vdW heterostructures comprising a vertical stack of different 2D materials have infinitely expanded the scope of custom designing a variety of devices with novel properties by manipulating the material and stacking sequence.[9] Overall, there have been significant advances in the field of metal nanostructures, especially in gold, due to potential high-impact applications in areas such as photonics, electronics, optical sensing/imaging, and drug delivery.[9−11] Because of its very strong relativistic effects and spin orbit coupling (SOC), 2D gold has received significant attention from both theoretical and experimental material scientists. Researchers have so far developed a range of gold nanostructures using various biological, photochemical, and wet chemical methods.[11−15] Recently, Ye et al. reported a facile strategy to synthesize two atomic layer thick free-standing gold structures with enhanced catalytic properties.[16] Zhu et al. reported their success in producing one-atom thick, 2D gold membrane with a hexagonal lattice embedded in a thicker gold film by in situ transmission electron microscopy straining of a gold film.[17] Forti et al. reported a semiconductor response for a stable 2D gold film sandwiched between silicon carbide and a monolayer of graphene.[18]

Several significant theoretical literature on 2D gold and gold clusters which prefer to be planar are already available.[19] Yang et al. have proposed four potentially viable 2D gold lattice structures (hcp, honeycomb, square, and tetracoordinate) with deep electronic property implications.[20] They showed that hcp gold (CPG) is the most stable in terms of cohesive energy and that it is metallic. Liu et al. extended the study and showed that honeycomb gold (HG) is energetically only slightly less stable than CPG and therefore equally probable.[21] They calculated

Received: November 2, 2022
Accepted: November 18, 2022
Published: December 1, 2022

https://doi.org/10.1021/acsami.2c19743
ACS Appl. Mater. Interfaces 2022, 14, 54992−55003

the electron density distribution (EDD) for HG, CPG and fcc gold. While both CPG and fcc gold showed a uniform spatial charge distribution, consistent with their metallic characteristic, EDD for HG showed directionality and covalent characteristics similar to that of graphene. Unlike graphene, their calculations also showed that HG is a semiconductor with a tunable bandgap based on whether it has an arm chair or zig zag structure, which are both probable. They attributed this rare semiconductor band structure of HG, a 2D transition metal, to its very strong SOC and hence an increased Coulombic interaction between the valence electrons and the nuclei resulting in band splitting. They showed that HG exhibits a covalent bonding characteristic and is a semiconductor with a band gap of 0.1−0.3 eV. Highlighting the critical importance of synthesizing the so-called "gapped" 2D transition metal crystals (e.g., HG) through their theoretical research, they noted that such solids have never been discovered. They recognized that the nondirectionality of metallic bonding severely restricted the application of the established synthetic routes for other 2D materials (e.g., graphene) to 2D transition metal crystals.

In our research, we specifically set out to close this gap in the field. Our experimental approach is based on the well-known phenomenon of "melting point depression" in high surface-to-volume ratio materials. According to the Lindemann criterion, a solid should start to melt when the amplitude of its atomic vibrations and nearest-neighbor distance (R_{IN}) become comparable.[22] Killean and Lisher reported a linear decrease in the melting point of metals with a decrease in their Debye temperatures.[23] It is also established that the vibrational amplitude of surface atoms of a crystalline material could be up to 100% higher than their bulk value, resulting in up to a 50% decrease in their surface Debye temperatures compared to their bulk temperatures. In other words, crystal surfaces would start to melt at temperatures that are significantly lower than their standard bulk melting temperatures. Frenken et al. were the first to report a partial disordering (melting) of the Pb(110) surface starting at 75% below its bulk melting point.[24] These findings were also corroborated by Breuer et al.[25] Ma et al. reported a range of surface Debye temperatures for polycrystalline gold films from 83 to 121 K as compared to their bulk value of 165 K.[26] De Los Santos et al. observed solid-state dewetting of gold films resulting in the formation of crystallites and island growth below 360 °C.[27] At temperatures greater than 360 °C, they observed that the gold film started to melt and diffuse on the surface to the crystallites. In our research, we developed a technique based on the phenomenon of surface melting point depression to synthesize one-atom thick gold (i.e., goldene) films and self-assembled 2D periodic goldene arrays. In this manuscript, we describe the goldene synthesis process and its novel properties and report on a special phenomenon of electric field-induced self-assembly of goldene.

EXPERIMENTAL METHODS

Film Deposition. Thermal evaporation process was used to deposit gold thin films onto sapphire substrates. High purity gold wire with a purity of 99.99% and a wire diameter of 2.0 mm was procured from Sigma-Aldrich. The sapphire film substrates were purchased from University Wafers Inc. USA. The sapphire substrates were single-crystalline, of *c*-axis (0001) orientation, and double-side polished with a diameter and thickness of 50.8 mm and 430 μm, respectively. Thermal evaporation system (Denton Vacuum LLC 502 B) was used to deposit the gold thin films onto freshly cleaned (after plasma treatment) sapphire substrates. A base pressure of ~3×10^{-7} torr was achieved prior to the deposition of the gold films. Prior to the evaporation process, a lower current of ~50 A was applied for a duration of 3 min for preconditioning the tungsten boat. We calibrated the film deposition rate of 1 Å/s at 72 Å by an in-built quartz crystal monitor (QCM) and maintained constant throughout the process. Gold films with different (QCM) thicknesses [e.g., 10, 25, 30, 50 nm (66 nm by X-ray reflectivity), 100 nm, and 200 nm] were deposited on the sapphire substrate. After the deposition of the gold films, the samples were diced into 5 mm × 5 mm square-shaped samples and heat-treated in a preheated oven (Carbolite 1200, UK). Postdeposition heat-treatment temperature ranged from 350 to 475 °C in air. The duration of heat treatment was 2, 5, 30, and 60 s.

Film Characterizations. *AFM Characterizations.* Atomic force microscopy (Park NX10, Park Systems, Korea), magnetic field microscopy (MFM), and conductive-atomic force microscopy (C-AFM) were extensively used to measure the surface topography of post heat-treated gold films. Super sharp standard NCH cantilevers were mounted on the Park AFM System, and AFM topography data were collected in a "true" non-contact mode. We acquired topography, phase, amplitude, and error scans simultaneously. Silicon cantileverss with resonant frequencies of 204−497 kHz and a force constant of 10−130 Nm^{-1} were used. The technical specifications of these probes were (i.e., thickness, length, width, and tip height) 4 ± 1 μm, 125 ± 10 μm, 30 ± 7.5 μm, and 10−15 μm, respectively. These probes have a typical tip radius of 2 nm. Cantilever amplitude of 20 nm was used in these measurements. AFM scans were collected at 512 × 512 pixel/lines with a scan speed of 0.30 at a fixed angle of 0°. AFM scan artifacts were minimized by acquiring the typical scan at an angle of 90° under identical scan parameters. All AFM scans were postprocessed by Gwyddion free software (version 2.55), an SPM data visualization and analysis tool.

In addition to conventional AFM imaging, the surface magnetic properties of gold films deposited on the sapphire substrate were examined by MFM attachment to the Park NX10 atomic force microscope. In this mode, we scanned the sample surface twice, that is, the tip scans the sample surface for topography information first followed by a second scan during which the tip scans the sample surface for magnetic signals at an increased tip-to-sample distance. In thin films, MFM is used to acquire an image map of the magnetic domain structures of the sample surface. In these experiments, we used a sharp tip coated with a soft magnetic thin film to enable measurement of magnetic domains in soft magnetic samples. We used magnetic tips with a low coercivity of ~0.75 Oe and remanence of 225 emu/cm^3 so that they could be magnetized and reoriented easily. The force constant and resonant frequency for these probes were 2.8 N m^{-1} and 75 kHz, respectively. The technical specifications of MFM probes were (i.e., thickness, length, and width) 3, 225, and 30 μm, respectively.

Additionally, Park NX10 AFM equipment was used for current versus voltage (I/V) spectroscopy on gold nanostructures. The low noise design feature of the system in the C-AFM option enabled us to precisely measure the extremely small changes in a sample's electronic characteristics. Pt−Si−NCH (conductive platinum silicide-coated silicon cantilevers) probes were used for C-AFM experiments. These probes were coated with the electrically conducting silicide coating on both sides, that is, the tip side as well as the detector side. The technical specifications of these probes were (i.e., thickness, length, width, and tip height) 4 ± 1 μm, 125 ± 10 μm, 30 ± 7.5 μm, and 10−15 μm, respectively. The resonant frequencies of 204−497 kHz and a force constant of 10−130 N m^{-1} were used. These probes could also be used for conductive AFM and tunneling AFM applications. IV spectroscopy was carried out in more than five different locations on the same sample and were also repeatable in the different samples over a closed cycle voltage range from +10 to −10 V and vice versa.

Chemical and Structural Characterization (EDS/TEM/SAED). Surface morphology of the heat-treated gold films deposited on sapphire was analyzed by field emission scanning electron microscopy (Quanta FEG 450). Energy-dispersive X-ray analysis (EDS) was performed using scanning electron microscopy (SEM) in an attachment at 10 kV accelerating voltage and ~10 mm working

https://doi.org/10.1021/acsami.2c19743
ACS Appl. Mater. Interfaces 2022, 14, 54992−55003

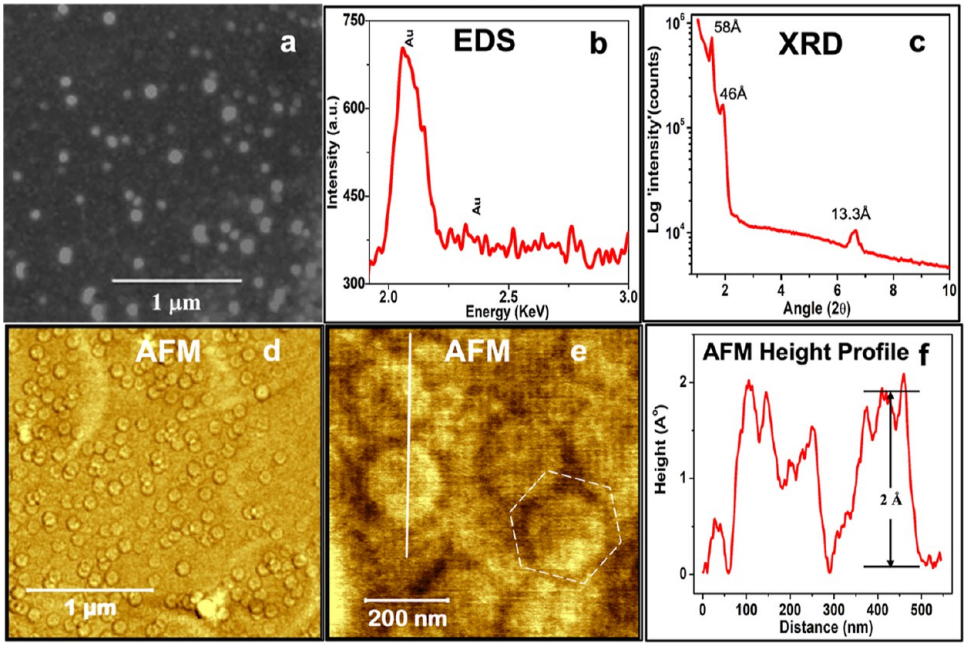

Figure 1. Characterization of the heat-treated gold film on sapphire: (a) SEM image of a region of the heat-treated gold film on sapphire.(b) EDS spectra of the region in (a) confirming that it is a gold film. (c) Low-angle XRD spectrum of the film with peaks at 58, 46, and 13.3 Å indicating apparent long-range superlattice ordering. (d) AFM image where we show the ubiquitous presence of hexagonal gold crystallites. (e) High-magnification AFM image of these hexagonal-shaped gold crystals. The height profile of two gold crystals [white line in (e)] is shown in (f) to be ∼2 Å.

distance in high vacuum operation. X-ray diffraction (XRD) measurements were carried out using a Panalytical Empyrean X-ray diffractometer equipped with a Cu anode X-ray tube operated at 45 kV and 40 mA in Bragg−Brentano geometry. TEM samples were characterized using a Talos F200X FEG transmission electron microscope with a lattice-fringe resolution of 0.14 nm at an accelerating voltage of 200 kV equipped with CETA 16M camera. High-resolution images of periodic structures were analyzed using TIA software.

X-ray photoelectron spectroscopy (XPS) was used to characterize the goldene samples synthesized on sapphire substrates for their chemical composition and surface chemical states. We used an AXIS Ultra DLD instrument with monochromatic Al Kα radiation with an energy of 1486.3 eV. The X-ray source was operated at a power of 117 W. XPS survey spectra were collected in the range of 0−1200 eV with a pass energy 160 eV. The chemical composition was ensured by collecting the high-resolution X-ray photoelectron spectroscopy (HR-XPS) spectra for Au 4f, Al 2p, O 1s, and C 1s in their binding energy ranges. All HR-XPS spectra were collected at a pass energy of 20 eV with a step size of 0.1 eV, and hence we only include the HR-XPS spectra recorded for Au 4f in the binding energy. Ar^+ ions with an energy of 4 keV with a current of 50 μA were used for a duration of 10 s to clean the sample surface contaminants. C 1s spectrum with a binding energy of 284.6 eV was used as reference with ±0.1 eV accuracy. The exact location of the binding energy peak positions was confirmed by fitting the HR-XPS data in the Lorentzian peak fitting model.

RESULTS AND DISCUSSION

Based on the literature observations, we hypothesized that exposure of a gold thin film sample deposited on a substrate (e.g., sapphire) to an optimum temperature and duration would lead to (partial) melting/disordering of its surface. It will trigger the following phenomenon: first, the film will start to recede from the substrate−film interface; the resulting decrease in surface energy and the associated higher melt/solid equilibrium temperature would lead to recrystallization of gold on the substrate. The resulting cycle of recurrent melting and recrystallization should create an instability at the film/substrate interface which would be resolved if the recrystallization process produced a stable 2D structure of gold, namely, goldene, because by definition, it does not have any "bulk." Guided by this hypothesis, we carried out experiments to successfully synthesize one-atom thick crystalline goldene structures exhibiting several unique properties.

As a first step, we determined the optimum temperature for goldene formation through a series of screening experiments in which a thin film of gold (Figure S1) on a single crystal sapphire (0001) substrate was exposed to temperatures of 350, 425, and 475 °C separately for 60 s. We observed typical solid-state dewetting of the films at 350 and 425 °C when the film separated into several small crystallites. In contrast, 2D nanostructures of gold were formed at 475 °C, and no solid-state dewetting was observed (Figure S2). Heat treatment durations greater than 60 s resulted in the complete melting of the films that is qualitatively consistent with the literature observations.

Analytical Characterization of Heat-Treated Gold Films on Sapphire. In Figure 1, we show results from the heat-treated film deposited on sapphire prior to any further processing. SEM imaging (Figure 1a) revealed the ubiquitous presence of small hexagonal crystallites. We also observed regions of honeycomb-structured gold film as shown in Figure S3. Figure 1b shows the EDS spectra of a region in Figure 1a confirming that it is a gold film. Low-angle XRD spectrum of the film (Figure 1c) showed peaks at 58, 46, and 13.3 Å, indicating an apparent long range superlattice ordering. XRD of the film confirmed the presence of gold with (200) and (220) diffraction peaks (Figure S4), and diffraction peaks for the sapphire substrate were also observed. High-magnification AFM imaging of regions in Figure 1d revealed an ordered hexagonal array of one-atom thick (i.e., ∼2 Å) gold crystals

https://doi.org/10.1021/acsami.2c19743
ACS Appl. Mater. Interfaces 2022, 14, 54992−55003

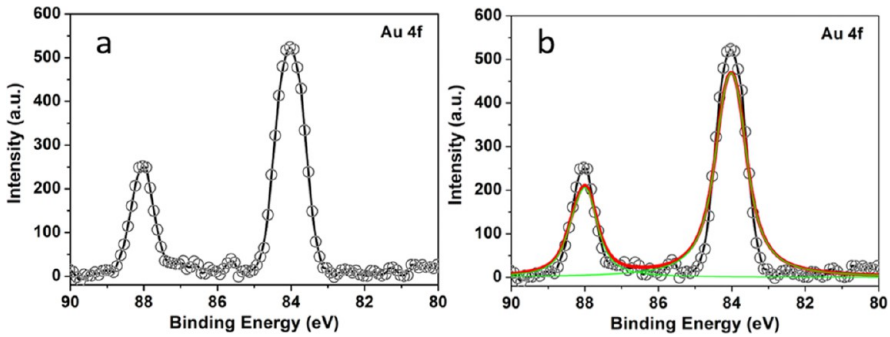

Figure 2. HR-XPS spectrum collected for gold films: (a) Au (4f) and (b) Au (4f) with the Lorentzian peak fitting model. Au (4f) high-resolution spectrum shows two well-defined peaks located at the binding energies of 84.02 and 88.04 eV corresponding to Au $4f_{7/2}$ and Au $4f_{5/2}$, respectively.

(Figure 1e,f).[4,13,14,16] The observation of hexagonal crystallites in AFM studies is consistent with the SEM observations (Figure 1a). Detailed AFM characterizations of the heat-treated gold film on sapphire are also shown in Figure S5.

XPS Characterization of Heat-Treated Gold Films. HR-XPS spectrum is collected for Au (4f) as shown in Figure 2. Figure 2a represents the HR-XPS spectra collected for Au (4f) in the binding energy range of 80−90 eV. Two well-defined peaks located at 84.02 and 88.04 eV are observed. The detailed signature of spin states are estimated by deconvolution of binding energy peaks using the Lorentzian peak fitting model of the same HR-XPS spectrum (Figure 2b). The fitted curve is displayed in red line, while the green line shows the individual peak fitted in the Lorentzian fitting model.

Deconvolution of binding energy peaks showed 84.02 and 88.04 eV corresponding to Au $4f_{7/2}$ and Au $4f_{5/2}$, respectively.[28−30] Observation of the well-defined Au 4f doublet apparently implies a single chemical environment. Au $4f_{7/2}$ peak position is shifted to a higher energy level than that for metallic gold (i.e., 83.8 eV) by 0.22 eV.[18] This directional shift to higher energies for goldene is qualitatively consistent with the 0.6 eV shift reported in the literature for Au adatom clusters by Novotný et al., who also observed the standard peak position of metallic gold, namely, 83.8 eV, for thicker gold films.[29]

TEM Analysis. In Figure 3, we report the results of our extensive HRTEM characterization of goldene films in the bright field mode. In the bright field mode of imaging, the incident beam direction is normal to the specimen surface and the atomic positions realized by HRTEM imaging in the same regions. Figure 3a is the low-magnification image of the goldene film, and Figure 3b shows the selective area electron diffraction (SAED) pattern data of the film. It can be inferred from the respective d-spacing of 2.40, 2.05, and 1.467 Å (JCPDS card no. 04-0784) that these (hkl) values correspond to the observed (111), (200), and (220) reflections of fcc gold. Figure 3c is the higher-magnification image of the marked region of Figure 3a, showing a crystalline lattice. In the inset of Figure 3c, we show the fast Fourier transform (FFT) viewed along the [011] zone axis from the marked region in Figure 3c. These lattice directions of (200), $(1\bar{1}1)$, and $(11\bar{1})$ are consistent with those of fcc gold. Figure 3d is the magnified lattice image of the region within the white box in Figure 3c, revealing a highly ordered structure with a spacing of 0.24 nm as indicated by the two parallel white dashed lines. In some locations, we measured a slightly larger lattice spacing of 0.26 nm attributed to possible strain in the goldene films during the film transfer process. We observed (200) fcc and (0001) honeycomb (white box) lattice structures across the entire image field. The fcc lattice plane directions (200), $(1\bar{1}1)$, and $(11\bar{1})$ are marked on the crystalline lattice with yellow lines with 55.7° angles between them. The increase in the interplanar angle ∼1° from the standard angle of 54.7° might also be ascribed to the lattice strain. Figure 3e is an inverse FFT (IFFT) image of a region in Figure 3d, confirming the predominance of honeycomb (white box) lattices. We observed the ubiquitous presence of lattice transformation between honeycomb goldene (HG) and close packed goldene across the image field. The extraction of (0001) hcp and (200) fcc lattice planes onthe IFFT image demonstrates the possibility of hcp to fcc transformation due to uniaxial compression of hcp along *c*-axis transformation to a (200) plane of fcc.[31]

Additional HRTEM image, collected from another region in the goldene film (Figure 3f), again confirmed the presence of a highly ordered crystalline lattice across the image field. Inset of the Figure 3f reveals FFT extracted from the marked region (Figure 3f) with lattice spacings of 0.248, 0.24, and 0.23 nm that is consistent with the fcc Au single-crystal structure. Figure 3g is a high-magnification image from inside the white square in Figure 3f, showing several honeycomb lattices highlighted by white hexagonal boxes. A lattice spacing of 0.24 nm is again measured as indicated by the two parallel white dashed lines. At some locations, we do see a change in the d spacing by ±0.02 nm.

A possible reason for the smaller goldene lattice spacing than the reported 0.26 nm value for gold clusters by Westenfelder et al. is unclear but might again indicate a more compressed goldene axial plane.[32] The smaller lattice spacing of 0.24 nm, however, is consistent with the recently reported values of 0.237−0.239 nm for the simple hexagonal lattice of one-atom thin gold film synthesized by a mechanical thinning process by Zhu et al.[17] Their findings are found to be consistent with our observation of smaller lattice spacing. The observation of smaller lattice spacing is likely due to the strong electron affinity to the nucleus and hence a dense electronic structure of goldene. Because of relativistic effects, it is known that gold exhibits strong SOC and increased Coulombic attraction between valence electrons and nuclei. The localization of electrons and the associated strong electron−electron (Coulombic) interactions in the goldene axial lattice plane would likely result in a significantly compressed lattice.

Figure 3h is an IFFT image of a region in Figure 3f where we clearly observed several regions showing herringbone and honeycomb structures. Herringbone to fcc (200) or (100) to herringbone to fcc (200) transition lattices are highlighted by

https://doi.org/10.1021/acsami.2c19743
ACS Appl. Mater. Interfaces 2022, 14, 54992−55003

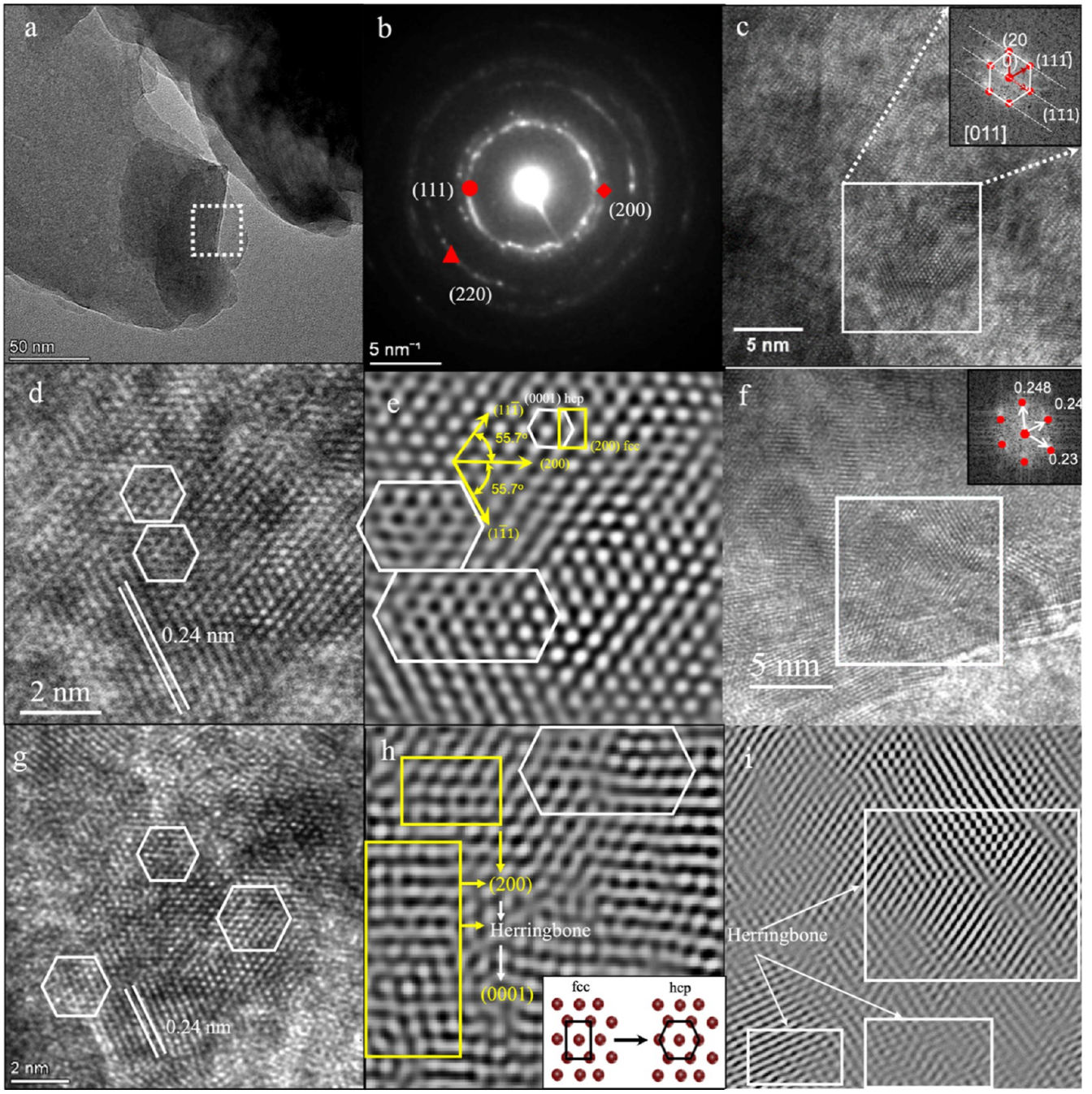

Figure 3. TEM characterization: (a) Low-magnification TEM image of a goldene film. (b) SAED pattern collected from a marked region in (a). SAED pattern detects the presence of (111), (200), and (220) reflections of fcc gold. (c) Higher-magnification image of the goldene film demonstrating the lattice fringes across the image field. Inset of (c) shows the FFT from the marked region viewed along the [011] zone axis. Presence of (200), $(1\bar{1}1)$, and $(11\bar{1})$ planes are consistent with fcc gold. (d) HRTEM image taken from the marked region from (c). Two parallel white dashed lines reveal 0.24 nm lattice spacing (d-spacing). (e) IFFT image extracted from the marked region in (c). IFFT image confirms the predominance of honeycomb structures marked with white ink. The lattice further shows an interplanar angle of 55.7° consistent with fcc gold. The (0001) hcp, (001), and (110) fcc lattice planes are marked on the IFFT image as well. (f) HRTEM image collected from another region in the goldene film showing a highly ordered crystalline lattice across the image field. Inset of (f) shows FFT extracted from the marked region. (g) High-magnification image collected from the marked region in (f). It shows several marked honeycomb lattice structures. (h) IFFT image from the marked region in (f). Inset of (h) shows the schematic illustration of possible fcc to hcp transformation due to uniaxial tension along a close packed direction in a basal plane of fcc followed by compression along c-axis transformation to a (0001) plane of hcp. Several hcp to fcc (200) transition lattices (yellow boxes) and herringbone to (200) fcc transitions (white boxes) are observed. Similar observation was also marked in (e). (i) IFFT image of the region extracted from the marked region (f) depicting several herringbone structures.

the yellow boxes. Honeycomb/herringbone to (200) transition lattices are highlighted by the white box. We also constructed a schematic illustration (inset of the Figure 3h) of possible hcp to fcc transformation due to uniaxial tension along a close packed direction in the basal plane of hcp. It demonstrates a compression along the c-axis in hcp (0001) transformation to a

https://doi.org/10.1021/acsami.2c19743
ACS Appl. Mater. Interfaces 2022, 14, 54992−55003

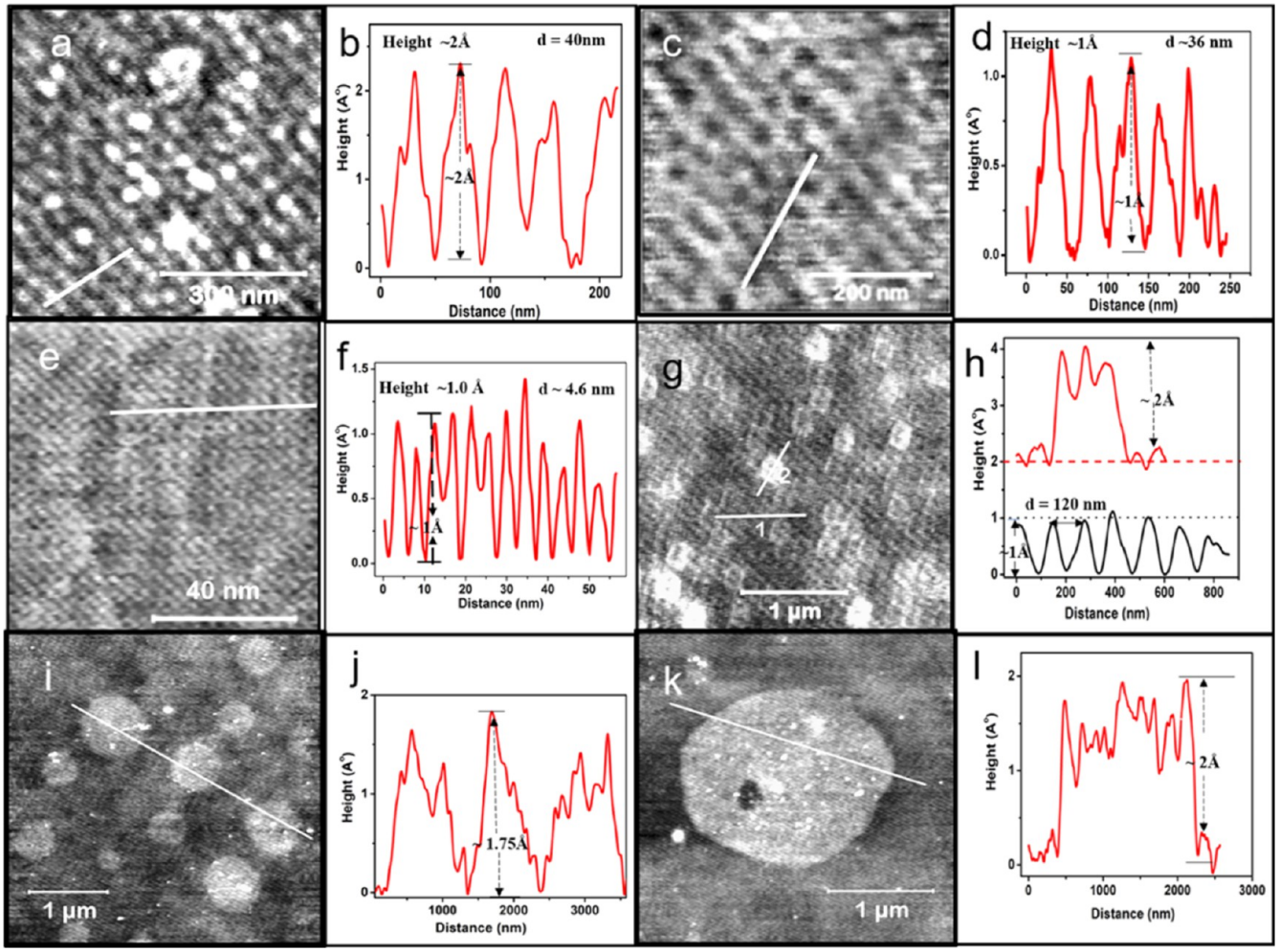

Figure 4. AFM analysis: (a) AFM image of an ordered, 1D (super lattice) array of one-atom thick gold with an approximate thickness of 2 Å (b). The approximate d-spacing of the superlattice is 40 nm. (c) Hexagonal network of one-atom thick (~1 Å) 2D gold with a super lattice spacing of ~36 nm (d). (e) Fine 2D ordered array of gold with an approximate thickness of 1 Å (f). The approximate d-spacing of the superlattice is 4.6 nm. (g,h) One-atom thick (~1 Å) 2D cubic superlattice array of gold with a d-spacing of 120 nm. The black line in (h) corresponds to the height profile across the white line labelled 1 in (g). The red height profile in (h) corresponds to the white line labelled 2 in (g) showing the growth of a second layer of cubic goldene crystal with a height of 2 Å. In (i,j), we observe several distinct, one-atom thick gold crystals with a thickness of ~1.75−2 Å. (k) High-magnification image of a 2 μM sized goldene crystal with a thickness of 2 Å (l).

(100) plane of fcc. Figure 3i is an IFFT image extracted from a region within the white box in Figure 3f. We could clearly see the presence of herringbone structures (white boxes) in the entire image field.

Our observation of the herringbone goldene lattice is consistent with the well-established phenomenon of gold surface layer reconstruction to form herringbone structures.[33] The strained boundaries on the crystal surface between the predominant fcc and the compressed hcp result in the formation of ridges with the herringbone structure. The pioneering STM work by Barth et al. also confirmed the presence of (herringbone) superlattices arranged in a zigzag fashion with a bending angle of 120° at every 250 Å. Moreover, Xiao et al. reported that zigzag structures (i.e., herringbone) are the most energetically stable for planar gold clusters in comparison to linear and square forms and for Au_3 clusters calculated at a bend angle of 137°.[34] We will share more data on electric field-induced self-assembled zigzag herringbone structures in the section on e-printing of goldene.

Our observation of the prevalence of honeycomb goldene lattice is consistent with the predictions of Liu et al.[21] Based on their energy and dynamic analysis calculations, they concluded that a one-atom thin 2D gold with a honeycomb structure (HG) is stable from a thermodynamic and lattice dynamic viewpoint. They also noted that 2D close packed gold (CPG) is energetically only slightly more stable, implying that both structures should be equally probable. Recently, Li and Ding reported the criteria for the stability of herringbone structures on reconstructed gold surfaces.[35] Their research revealed that lattice deformation of the bulk atomic layers in three-dimensional gold crystals with more than 12 atomic layers was required for the relaxation and stability of the anisotropic gold surface layer structures, namely, the herringbone. In other words, in the absence of a minimum of 12 atomic layers of gold, the herringbone structure might not be stable. Implication of this important result for goldene can be explained as follows: the nuanced logic regarding the stability of herringbone structures in goldene is buried in the fact that they are formed as relief ridges at the strained boundaries (between fcc and compressed hcp) on the crystal surface. As per Liu et al. predictions, we observed a dynamic transition between HG and CPG structures (i.e., they are equally

https://doi.org/10.1021/acsami.2c19743
ACS Appl. Mater. Interfaces 2022, 14, 54992−55003

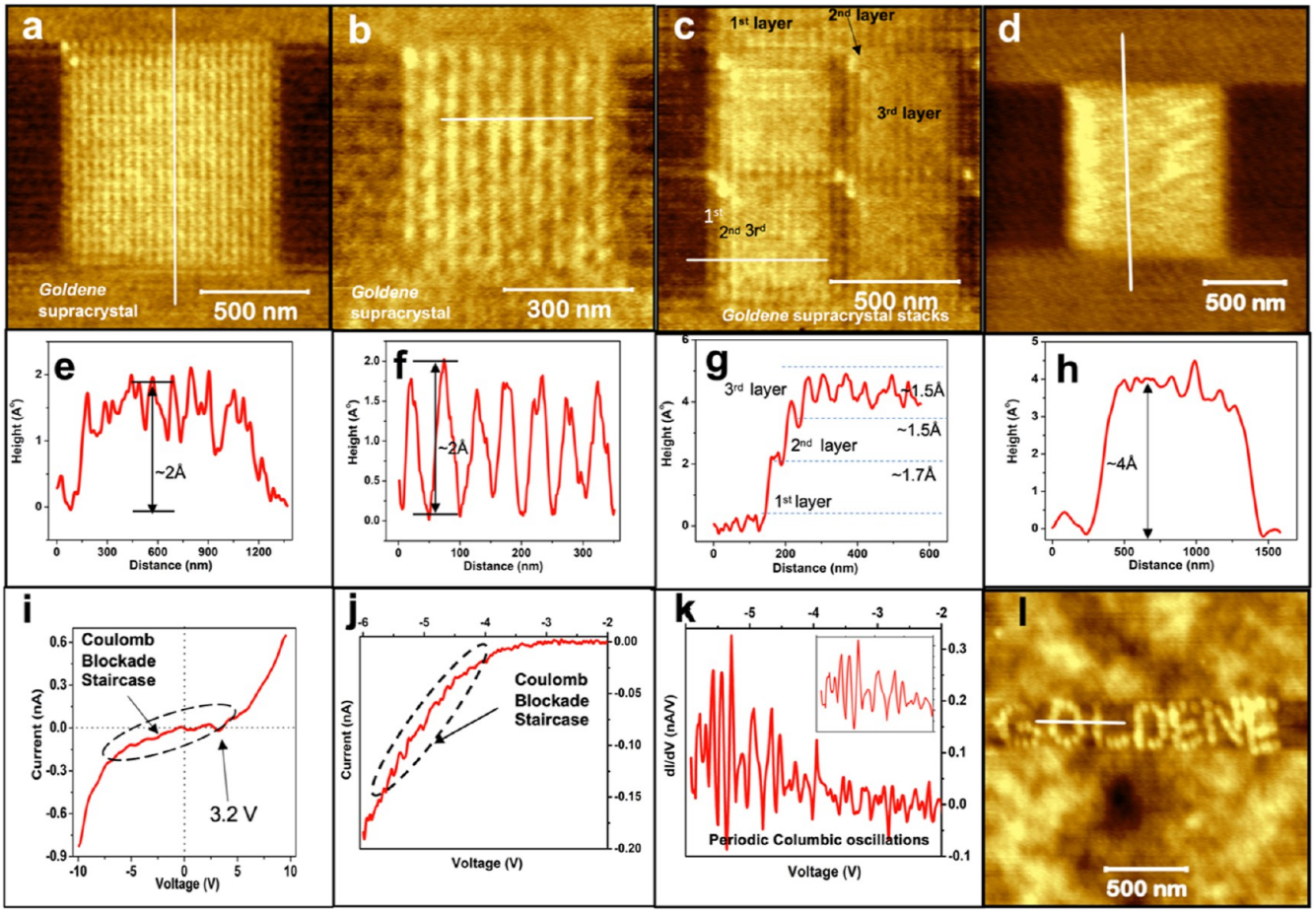

Figure 5. Electric field-induced self-assembly: (a,b) AFM images of 1 μm and 500 nm square electric field-induced self-assembled goldene supracrystals. Height profiles extracted from (a,b) are also shown in (e,f), respectively. (c) AFM image of a vertical stack of three goldene supracrystal layers. The third layer comprises four 400 nm square goldene supracrystals. These vertical stacks are clearly observed in the height profiles shown in (g). (d) AFM image of a two-atom thick, 1 μm square gold supracrystal. (h) Height profile along the white line in (d). (i) *IV* profile of a goldene film, showing a typical Schottky characteristic with a knee voltage of ~3.2 V. In (j), we show another goldene *I*−*V* profile with a clear demonstration of the Coulomb staircase phenomenon. The periodicity of the Coulomb oscillations is shown in (k) by plotting the slope of the *IV* curve [shown in (j)] as a function the applied voltage. The inset of (k) shows the zoomed image of a region in the figure. In (l), we show the AFM image of the word GOLDENE printed using an electric field-induced self-assembly of goldene.

probable), with herringbone ridges as a common feature for goldene (Figure 3h,i).[21] It is therefore logical for us to conclude that goldene would exhibit a dynamic (i.e., temporal) areal distribution of CPG, HG, and herringbone structures. The question of stability of herringbone structures for goldene would therefore appear to be moot. The fluidlike nature of goldene is an active topic research for us, and we hope to report our findings in the near future. In Figure S6, we show the extended STEM/HAADF EDS data of goldene films, once again confirming gold.

We are apparently the first group to synthesize stable honeycomb-structured goldene and demonstrate that it is a semiconductor. We will discuss the semiconducting property of goldene in a later section of the manuscript. It is truly remarkable that in our study, HRTEM lattice imaging of goldene revealed both herringbone and honeycomb lattices, which can only be observed at the gold surface due to its reconstruction. Imaging of these gold surface-only features by a nonsurface characterization technique such as HRTEM is an unequivocal proof for the absence of three-dimensionality of goldene.

AFM Analysis. In this section, we report the results of our extensive AFM characterization of goldene films confirming that they are one-atom thick (~2 Å) crystals. Free-standing goldene films were transferred and solution cast from the heat-treated samples. AFM analysis of these films (Figure 4) revealed the ubiquitous presence of self-assembled 1D and 2D (hexagonal) superlattice arrays and single crystals of goldene. A one-atom thick (~1 to 2 Å), 1D goldene array with a d-spacing of ~40 nm (~30× of the 13.3 Å peak reported in Figure 1b) is shown in Figure 4a,b. A hexagonal, 2D array with a thickness of ~1 Å and a d-spacing of ~36 nm (~27× of the 13.3 Å peak observed Figure 1b) is shown in Figure 4c,d. Figure 4e is a high-magnification image of a 1 Å thick supracrystalline array with a d-spacing of 4.6 nm (Figure 4f) that is consistent with the second order peak of 46 Å reported in Figure 1b. We show a 3 μm scan image of a 1 Å thick cubic, superlattice array with a periodicity of ~120 nm along the white line labelled 1 in Figure 4g and the black line in Figure 4h (~26× of the 46 Å peak in Figure 1c). AFM measurements of less than 2 Å (e.g., 1 Å) imply that the AFM tip did not completely reach the bottom of the goldene array. We observed the nucleation and growth of a second layer of cubic crystals on top of the first

https://doi.org/10.1021/acsami.2c19743
ACS Appl. Mater. Interfaces 2022, 14, 54992−55003

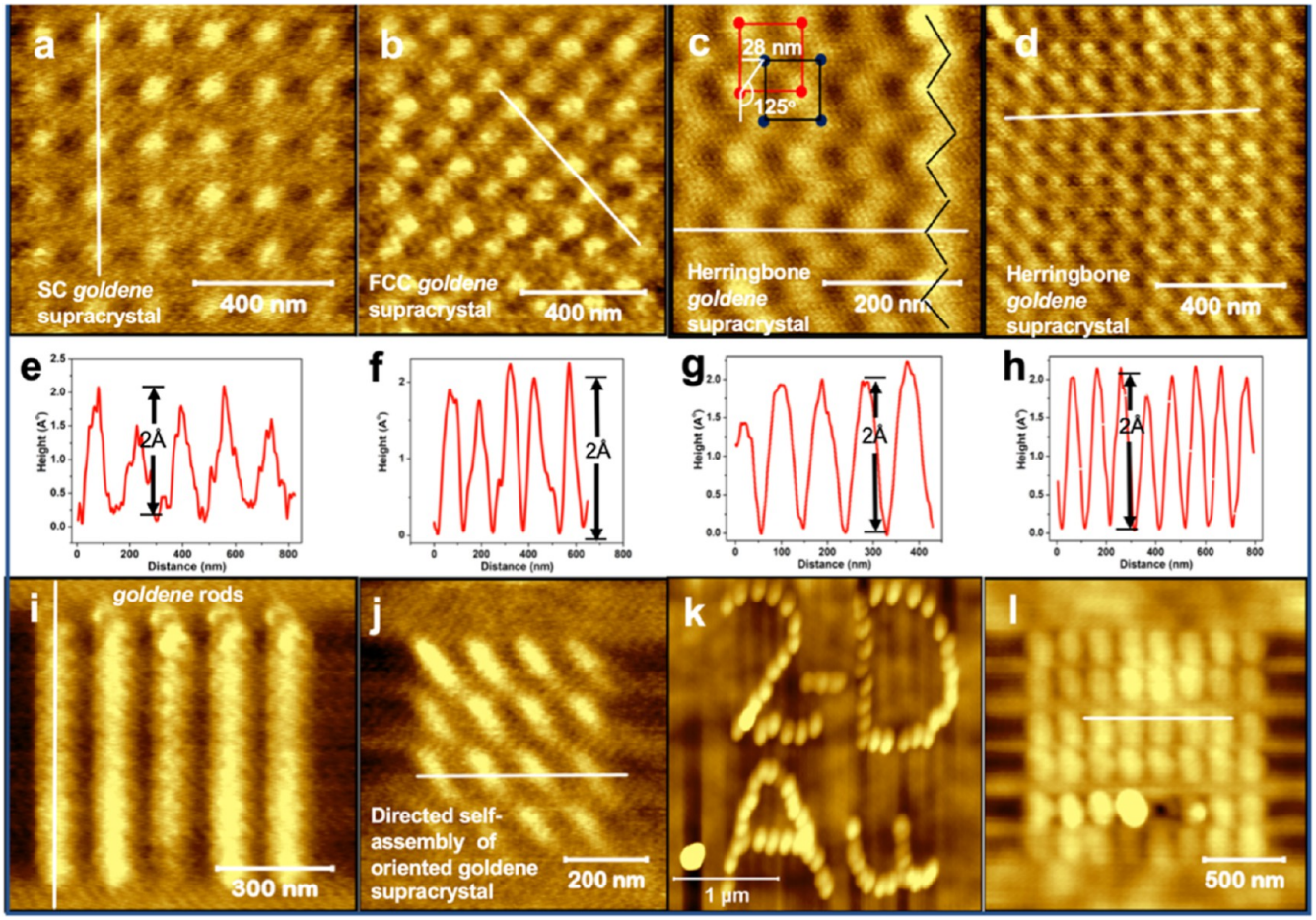

Figure 6. Supracrystalline structure: (a,b,e,f) E-printed (1 μm × 1 μm) SC and FCC goldene supracrystals. When the d-spacing was reduced to <100 nm, the SC array transformed into a herringbone structure as shown in (c,d,g,h) with a bend angle of 125° at every 28 nm. (i,j) E-printed goldene rods and self-assembled oriented ellipsoidal arrays, the latter indicating goldene magnetism. (k,l) Sub-nm thick e-printed letters and patterns on a goldene film synthesized on silicon.

layer with a thickness of 2 Å (white line labelled 2 in Figure 4g and red line in Figure 4h). Several well-formed and distinct goldene crystals that are ~2 Å thick are observed (Figure 4i,j).

In Figure 4k, we show a higher-magnification image of a 2 Å thick crystal (Figure 4l). Additional data on goldene superlattices and 2D crystals that are several micrometers long are shown in Figures S7 and S8). In Figure S9, we show error maps observed in the AFM thickness measurement data shown in Figure 4a,c,e,k, namely, ±10, ±5, ±10, and ±10 pm. They are very small compared to the measured thicknesses.

Electric Field-Induced Self-Assembly—e-Printing. In this section, we report on the effect of applying a localized electric field to goldene films using the C-AFM feature in the AFM system. "Ultimate low-noise conductive" AFM mode was used to suppress the electrical noise in the order of a few femto-amperes. Goldene samples were prepared by "drop casting" the dispersion onto a clean silicon wafer. C-AFM cantilever tip was used to subject specific locations on the film to a voltage sweep over a given duration of time. Voltage ranges between +10 and −10 V and sweep times of 0.5−15 s were used. This process resulted in the nucleation and self-assembly of discrete goldene structures at these locations. Optimization of the process resulted in the synthesis of a variety of self-assembled goldene structures (Figures 4 and 5), namely, supracrystals, simple cubic (SC), face centered cubic (FCC), herringbone arrays, oriented ellipsoidal structures, and rods. We were also able to print/record stable sub-nanometer thick patterns and texts.

Some examples of electric field-induced self-assembly of goldene supracrystals are shown in Figure 5a−d with their height profiles listed in Figure 5e−h, respectively. In Figure 5a,b,e,f, we show 1 μm × 1 μm and 500 nm × 500 nm size, one-atom thick goldene supracrystals with a simple cubic structure. In Figure 5c, we show the AFM image of a stack of three layers of 1 μm size goldene supracrystals. The third layer comprises a 2 × 2 matrix of 0.5 μm × 0.5 μm goldene pixels. Figure 5g clearly shows the stepped height profile of the three-layer stack along the white line marker in Figure 5c. Measured steps heights of ~1.7, 1.5, and 1.5 Å confirmed that these are one-atom thick goldene supracrystals. In Figure 5d, we show an image of 1 μm × 1 μm sized gold supracrystal with a measured height of 4 Å along the white line, as shown in Figure 5h. It is a two-atom thick goldene crystal.

A closer look at the current/voltage (*IV*) data obtained during the voltage sweep revealed two remarkable findings. First, we observed a semiconductor response from goldene exhibiting a typical Schottky *IV* characteristic with a "knee voltage" of ~3.2 V (Figure 5i) which is qualitatively consistent with the predictions of Liu et al.[21] Second, we observed a stepwise *IV* characteristic (i.e., Coulomb staircase) between 0 and −10 V indicating a Coulomb blockade phenomenon.[36] Extensive experimentation confirmed the presence of periodic,

https://doi.org/10.1021/acsami.2c19743
ACS Appl. Mater. Interfaces 2022, 14, 54992−55003

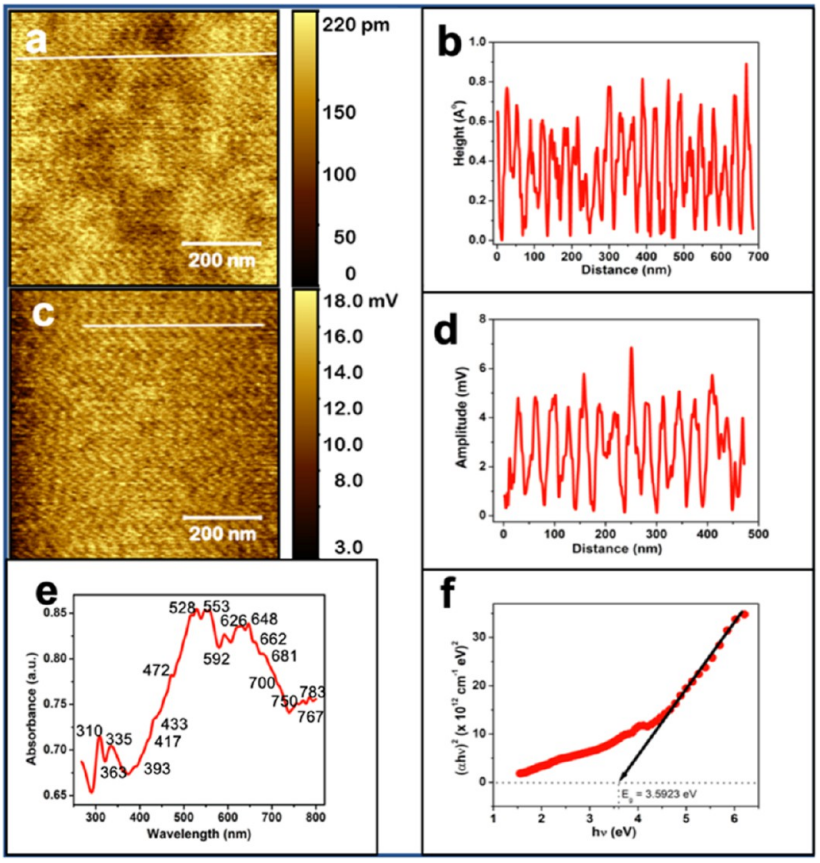

Figure 7. Magnetic and optical properties: (a) AFM image of the periodic goldene array that is one-atom thick measured along the white line marker [shown in (b)]. In (c), we show an MFM amplitude image of the goldene array shown in (a). A periodic pattern of the amplitude (mV) with distance is observed. In (d), we show the quantitative plot of the amplitude array along the white marker line in (c). It is consistent with the frequency of the topographic array in (a,b). In (e), we show the goldene optical absorption spectrum. Several well-resolved intense bands and some fine bands were observed. (f) shows the Tauc's plot, and we calculate the optical band gap for goldene to be 3.59 eV.

room-temperature Coulomb blockade oscillations manifest as Coulomb staircase in the current/voltage spectra (Figure 5j). The periodicity of the *IV* oscillations in Figure 5j was further confirmed by plotting the rate of change of current as a function of the applied voltage, that is, dI/dV versus V (Figure 5k), implying equally spaced charging peaks in an ideal Coulomb blockade context within goldene crystals. It is important to note that while the amplitude of the oscillations clearly increased with increasing magnitude of the applied voltage, the frequency of the oscillations seemed to remain constant.

The Coulomb blockade phenomenon in goldene could be better explained by the concept of electron localization in 2D crystals. We will rely primarily on the extensive DFT studies that already exist for gold clusters due to their extreme relevance to goldene. First, it is now very well established that energetically stable, 2D planar gold structures are predicted for cluster sizes of up to 12 atoms due to relativistic effects, thereby providing strong support for the existence of stable goldene. Second, one should not expect electron delocalization in goldene atoms because of the absence of a three-dimensional "bulk" phase, resulting in electrons being pinned at each atom. This is again well supported by the established literature in the field of electronic structure of gold clusters.[36] Moreover, static polarizability is a strong indicator of valence electron delocalization, and the electronic structure and DFT calculations reported by Li et al. clearly showed that it increased linearly with gold cluster size, confirming a strong electron affinity to the nucleus and a dense electronic structure. It is logical to infer that these observations would apply to goldene. While electrons in gold clusters with even number of atoms are paired up, odd numbered clusters have one unpaired electron and are therefore ferromagnetic.[37] Based on these observations, one could logically conclude that goldene crystals will be ferromagnetic. We will report on the observed magnetism of goldene in another section of the manuscript.

We therefore concluded that the phenomenon of localized electrons and the associated strong electron−electron (Coulombic) interactions in the axial lattice plane would lead to the observed Coulomb blockade effect and opening of the band gap for a Mott insulator (?). This would result in a highly compressed lattice along the axial plane and would explain our measurement of a smaller interatomic spacing of 0.24 nm compared to the reported 0.26 nm for 2D planar gold clusters. The continuous charging of the Coulomb blockaded goldene crystals during the I−V sweep should therefore result in equally spaced charging peaks (i.e., Coulombic oscillations) around the threshold voltage for electron flow, consistent with our observations.[38] The presence of localized charge accumulation (i.e., Coulomb islands) in goldene crystals, as supported by the spatial EDD distribution calculations by Liu et al.,[21] would further explain the electric field effect, namely, nucleation of stable goldene clusters and patterns by manipulation of these charges with the C-AFM probe. This

https://doi.org/10.1021/acsami.2c19743
ACS Appl. Mater. Interfaces 2022, 14, 54992−55003

is illustrated by our ability to e-print the word GOLDENE (Figure 5l). The AFM image of the region prior to e-field application and the height profiles of the GOLDENE letters are shown in Figure S10.

Supracrystalline Structures. In Figure 6 we report on our ability to extend the electric field effect to e-print several supracrystalline goldene structures. In Figure 6a,b,e,f, we show e-printed SC and FCC goldene structures that are 2 Å in thickness. For superlattice spacings that are less than 100 nm, the process of e-printing SC supracrystals produced 2 Å thick herringbone structures instead (Figure 6c,d,g,h), indicating further local charge redistribution in the Coulomb islands in the nucleation sites due to minimum energy requirements. We have discussed earlier in the manuscript the well-established phenomenon of the Au(111) surface layer reconstruction process to form a herringbone structure.[19]

Moreover, we measured the thickness of 2 Å and bending angles to be ∼125° across the length ∼28 nm (Figure 6c) which is consistent with the reported literature values for gold surface atoms and clusters.[33] It is important to reiterate that the herringbone structure is a surface atomic reconstruction phenomenon in gold, and observation of 1 μm 2 Å thick goldene supracrystals with a stable herringbone structure implies that these crystals are one-atom thick surfaces.

In Figure 6i, we show an ordered parallel array of goldene rods. In Figure 6j, we e-printed an oriented ordered array of ellipsoidal goldene crystals indicating goldene ferromagnetism. With electronic device/system applications in mind, we extended the e-printing technique to goldene films that were directly prepared on silicon by the heat treatment process. We printed the words "2D Au" (Figure 6k) and a periodic dot pattern of sub-nanometer thick goldene pixels (Figure 6l) on these films. In Figure S11, we show the height profiles along the line markers of images in Figure 6i,j,l. It is important to note this phenomenon was not observed in "as deposited" gold films (Figure S12). Figure S13 is the AFM image of a clean sapphire wafer.

Nanoscale Magnetism and Optical Properties. We used MFM and the well-established "dual pass" (lift mode) technique to characterize the nanoscale magnetism of the free-standing goldene films. Topographical data (AFM) by the true noncontact mode was obtained first, and deconvoluted magnetic gradient force field data (MFM) of the same region was obtained at a much larger tip/sample distance during the second scan. This process ensured the removal of any residual topographical contribution due to vdW forces from the MFM signal. Typically, we recorded the amplitude and phase information due to the long-range magnetic force (gradient) interaction between the gold sample and the cantilever tip.

In Figure 7a, we show the AFM topographic image of an ordered goldene array with a thickness of 0.8 Å (Figure 7b). Its magnetism was confirmed by the corresponding MFM amplitude image shown in Figure 7c. A tip/sample distance of 50 nm was used for the MFM scan. The magnitude of the amplitude signal is proportional to the intensity of the magnetic force exerted by the gold sample on the cantilever tip in the gradient field, and a peak amplitude of 5 mV was observed. The periodicity of the amplitude signal (Figure 7d) was consistent with that of the topographic signal. This was further confirmed by the corresponding MFM (phase) image shown in Figure S14. In Figure S15, we show an additional AFM topographic image and the corresponding MFM phase and amplitude images of goldene crystals, confirming their magnetism. In Figure S16, we show the topographic and MFM data of the standard test sample provided by the instrument manufacturer for calibration purposes.

Optical properties of gold nanoparticles are extremely well studied and exhibit an absorption band around 540 nm due to surface plasmon resonance. An interesting aspect of this phenomenon is the presence of a very strong UV band for small nanometer-sized gold clusters and for clusters of few gold atoms when the absorption phenomenon transitions from plasmon resonance to molecular absorption that is characteristic of their true electronic structure. We reiterate that it is widely accepted in the literature that gold clusters tend to remain planar up to 12 atoms.[39] Since our main focus for this manuscript is on one-atom thin goldene crystals, it is logical to assume that optical properties of planar gold clusters would be relevant to our study.

The optical absorption spectrum for goldene is shown in Figure 7e. We observed strong absorption bands around 310 nm (4.0 eV), 335 nm (3.7 eV), 528 nm (2.35 eV), 553 nm (2.24 eV), 592 nm (2.09 eV), 626 nm (1.98 eV), and 648 nm (1.91 eV) and several finer bands. These bands compared very well with the absorption bands of various gold clusters (Table S1) reported by Lecoultre et al.[40] Results of their extensive study of optical absorption of small gold clusters (Au_n: n = 1−5 and 7−9) frozen in neon at 7 K revealed a large number of transitions across a wide UV−vis energy range. Similar to our results for goldene, they also observed a number of intense and highly resolved bands and fine structures. We used the Tauc plot to calculate the optical band gap of goldene to be 3.59 eV (Figure 7f) which is consistent with the optical band gap value of ∼3.5 eV for gold clusters containing up to eight atoms, as reported by Koppen et al.[39]

CONCLUSIONS

HRTEM, SAED, HR-XPS, AFM, XRD, SEM, and EDS were used to unequivocally confirm the synthesis of free-standing, one-atom thick goldene crystals and self-assembled 1D and 2D goldene superlattice arrays. HRTEM lattice imaging of goldene revealed herringbone and honeycomb lattice structures, which are only to be observed at the gold surface due to its reconstruction. Imaging of such surface-only features by a nonsurface characterization technique such as HRTEM unequivocally confirmed the absence of the three-dimensionality of goldene. We discovered the phenomenon of electric field-induced self-assembly of goldene supracrystals (e.g., herringbone structures) and developed a technique to e-print goldene arrays and texts. Self-assembly transformation of e-printed goldene SC supracrystal to herringbone structures for lattice spacings <100 nm confirmed that they are essentially one-atom thick surfaces. Goldene has an optical band gap of 3.59 eV and exhibited multiple intense and highly resolved absorption peaks and finer bands across a wide energy range that is consistent with the optical properties reported for gold clusters. It is a semiconductor with a knee voltage of ∼3.2 V. Periodic room-temperature Coulomb blockade oscillations were observed as Coulomb staircase in the current/voltage characteristics. Goldene's nanoscale magnetism was confirmed by MFM.

Our ability to e-print (i.e., additive printing) sub-nanometer thick goldene pixels is expected to have profound implications in the fields of single electron tunneling device architecture and high-density information storage. The potential to leverage well-developed hard disk writing technologies to e-print

https://doi.org/10.1021/acsami.2c19743
ACS Appl. Mater. Interfaces 2022, 14, 54992−55003

goldene pixels should help facilitate ease of fabrication and commercialization of such systems. In principle, we anticipate extending the e-printing technology to include optical (e.g., laser) techniques to modulate the Coulomb islands in the goldene axial plane. We expect that publication of our goldene research will stimulate significant interest in the advanced materials research community.

■ ASSOCIATED CONTENT

Supporting Information

The Supporting Information is available free of charge at https://pubs.acs.org/doi/10.1021/acsami.2c19743.

Additional analytical characterization data—XRD, SEM, AFM, MFM, and UV−vis (PDF)

■ AUTHOR INFORMATION

Corresponding Author

Ramesh Jagannathan − *Engineering Division, New York University Abu Dhabi, Abu Dhabi 129188, United Arab Emirates;* orcid.org/0000-0003-0269-6446; Email: rj31@nyu.edu

Authors

Sudhir Kumar Sharma − *Engineering Division, New York University Abu Dhabi, Abu Dhabi 129188, United Arab Emirates*

Renu Pasricha − *Core Technology Platform, New York University Abu Dhabi, Abu Dhabi 129188, United Arab Emirates*

James Weston − *Core Technology Platform, New York University Abu Dhabi, Abu Dhabi 129188, United Arab Emirates*

Thomas Blanton − *International Centre for Diffraction Data, Newtown Square, Pennsylvania 19073, United States*

Complete contact information is available at: https://pubs.acs.org/10.1021/acsami.2c19743

Author Contributions

R.J. developed the concept behind the experiments, designed the experimental plans, and wrote the manuscript. S.K.S. carried out all experiments, and S.K.S. and R.J. shared the AFM characterization responsibilities and analyses. R.P. did the TEM characterization. J.W. did the XRD characterization. T.B. analyzed the XRD data and wrote the sections on XRD.

Notes

The authors declare no competing financial interest.

All data generated or analyzed during this study are included in this published article (and its Supporting Information).

■ ACKNOWLEDGMENTS

We acknowledge Prof. Erio Tossati [SISSA (Scuola Internazionale Superiore di Studi Avanzati) and ICTP (The Abdus Salam International Centre of Theoretical Physics)] for his keen insights and comments. We acknowledge the valuable support provided by the Core Technology Platforms at NYU Abu Dhabi for the use of the instruments. We acknowledge Dr. Qiang Zhang, Core Technology Platform at NYU Abu Dhabi for *IV* characterization of as-deposited gold films. We acknowledge the editorial support provided by Phillip Rodenbough at NYU Abu Dhabi.

■ REFERENCES

(1) Lee, C.; Wei, X.; Kysar, J. W.; Hone, J. Measurement of the Elastic Properties and Intrinsic Strength of Monolayer Graphene. *Science* **2008**, *321*, 385−388.

(2) Lai, A.; Du, Z.; Gan, C. L.; Schuh, C. A. Shape Memory and Superelastic Ceramics at Small Scales. *Science* **2013**, *341*, 1505−1508.

(3) Ahn, J. R.; Yeom, H. W.; Yoon, H. S.; Lyo, I. W. Metal-Insulator Transition in Au Atomic Chains on Si with Two Proximal Bands. *Phys. Rev. Lett.* **2003**, *91*, 196403.

(4) Rodrigues, V.; Fuhrer, T.; Ugarte, D. Signature of Atomic Structure in the Quantum Conductance of Gold Nanowires. *Phys. Rev. Lett.* **2000**, *85*, 4124−4127.

(5) Ahn, E. C. 2D Materials for Spintronic Devices. *npj 2D Mater. Appl.* **2020**, *4*, 17.

(6) Liu, C.; Chen, H.; Wang, S.; Liu, Q.; Jiang, Y. G.; Zhang, D. W.; Liu, M.; Zhou, P. Two-Dimensional Materials for next-Generation Computing Technologies. *Nat. Nanotechnol.* **2020**, *15*, 545−557.

(7) Chhowalla, M.; Jena, D.; Zhang, H. Two-dimensional semiconductors for transistors. *Nat. Rev.* **2016**, *1*, 16052.

(8) Gibertini, M.; Koperski, M.; Morpurgo, A. F.; Novoselov, K. S. Magnetic 2D Materials and Heterostructures. *Nat. Nanotechnol.* **2019**, *14*, 408−419.

(9) Novoselov, K. S.; Mishchenko, A.; Carvalho, A.; Castro Neto, A. H. 2D Materials and van Der Waals Heterostructures. *Science* **2016**, *353*, aac9439.

(10) Geim, A. K.; Grigorieva, I. V. Van Der Waals Heterostructures. *Nature* **2013**, *499*, 419−425.

(11) Anderson, D. G.; Burdick, J. A.; Langer, R. Smart Biomaterials. *Science* **2004**, *305*, 1923−1925.

(12) Lendlein, A.; Jiang, H.; Jünger, O.; Langer, R. Light-Induced Shape-Memory Polymers. *Nature* **2005**, *434*, 879−882.

(13) Huang, X.; Li, S.; Huang, Y.; Wu, S.; Zhou, X.; Li, S.; Gan, C. L.; Boey, F.; Mirkin, C. A.; Zhang, H. Synthesis of Hexagonal Close-Packed Gold Nanostructures. *Nat. Commun.* **2011**, *2*, 292−296.

(14) Xu, J.; Li, S.; Weng, J.; Wang, X.; Zhou, Z.; Yang, K.; Liu, M.; Chen, X.; Cui, Q.; Cao, M.; Zhang, Q. Hydrothermal Syntheses of Gold Nanocrystals: From Icosahedral to Its Truncated Form. *Adv. Funct. Mater.* **2008**, *18*, 277−284.

(15) Sasaki, K.; Okue, T.; Nakai, T.; Uchida, Y.; Nishiyama, N. Lateral Growth of Uniformly Thin Gold Nanosheets Facilitated by Two-Dimensional Precursor Supply. *Langmuir* **2021**, *37*, 5872−5877.

(16) Ye, S.; Brown, A. P.; Stammers, A. C.; Thomson, N. H.; Wen, J.; Roach, L.; Bushby, R. J.; Coletta, P. L.; Critchley, K.; Connell, S. D.; et al. Sub-Nanometer Thick Gold Nanosheets as Highly Efficient Catalysts. *Adv. Sci.* **2019**, *6*, 1900911.

(17) Zhu, Q.; Hong, Y.; Cao, G.; Zhang, Y.; Zhang, X.; Du, K.; Zhang, Z.; Zhu, T.; Wang, J. Free-Standing Two-Dimensional Gold Membranes Produced by Extreme Mechanical Thinning. *ACS Nano* **2020**, *14*, 17091−17099.

(18) Forti, S.; Link, S.; Stöhr, A.; Niu, Y.; Zakharov, A. A.; Coletti, C.; Starke, U. Semiconductor to Metal Transition in Two-Dimensional Gold and Its van Der Waals Heterostack with Graphene. *Nat. Commun.* **2020**, *11*, 2236−2237.

(19) Hanke, F.; Björk, J. Structure and Local Reactivity of the Au(111) Surface Reconstruction. *Phys. Rev. B: Condens. Matter Mater. Phys.* **2013**, *87*, 235422.

(20) Yang, L. M.; Dornfeld, M.; Frauenheim, T.; Ganz, E. Glitter in a 2D Monolayer. *Phys. Chem. Chem. Phys.* **2015**, *17*, 26036−26042.

(21) Liu, N.; Jin, S.; Guo, L.; Wang, G.; Shao, H.; Chen, L.; Chen, X. Two-Dimensional Semiconducting Gold. *Phys. Rev. B: Condens. Matter Mater. Phys.* **2017**, *95*, 155311.

(22) Wolf, G. H.; Jeanloz, R. Lindemann Melting Law: Anharmonic Correction and Test of Its Validity for Minerals. *J. Geophys. Res.* **1984**, *89*, 7821−7835.

(23) Killean, R. C. G.; Lisher, E. J. The Debye Temperatures of the Cubic Elements and Their Relationship to Melting Points. *J. Phys. C Solid State Phys.* **1975**, *8*, 3510−3520.

(24) Frenken, J. W. M.; Marée, P. M. J.; van der Veen, J. Observation of surface-initiated melting. *Phys. Rev. B: Condens. Matter Mater. Phys.* **1986**, *34*, 7506−7516.
(25) Breuer, U.; Knauff, O.; Bonzel, H. P. Surface Melting of Pb(110) Studied by x-Ray Photoelectron Diffraction. *Phys. Rev. B: Condens. Matter Mater. Phys.* **1990**, *41*, 10848−10851.
(26) Ma, W.; Zhang, X.; Takahashi, K. Electrical Properties and Reduced Debye Temperature of Polycrystalline Thin Gold Films. *J. Phys. D: Appl. Phys.* **2010**, *43*, 465301.
(27) De Los Santos, V. L.; Lee, D.; Seo, J.; Leon, F. L.; Bustamante, D. A.; Suzuki, S.; Majima, Y.; Mitrelias, T.; Ionescu, A.; Barnes, C. H. W. Crystallization and Surface Morphology of Au/SiO2 Thin Films Following Furnace and Flame Annealing. *Surf. Sci.* **2009**, *603*, 2978−2985.
(28) Boyen, H. G.; Ethirajan, A.; Kästle, G.; Weigl, F.; Ziemann, P.; Schmid, G.; Garnier, M. G.; Büttner, M.; Oelhafen, P. Alloy Formation of Supported Gold Nanoparticles at Their Transition from Clusters to Solids: Does Size Matter? *Phys. Rev. Lett.* **2005**, *94*, 016804.
(29) Novotný, Z.; Argentero, G.; Wang, Z.; Schmid, M.; Diebold, U.; Parkinson, G. S. Ordered Array of Single Adatoms with Remarkable Thermal Stability: Au/Fe 3O 4(001). *Phys. Rev. Lett.* **2012**, *108*, 216103.
(30) Barr, T. L. An ESCA Study of the Termination of the Passivation of Elemental Metals. *J. Phys. Chem.* **1978**, *82*, 1801−1810.
(31) Li, Q.; Niu, W.; Liu, X.; Chen, Y.; Wu, X.; Wen, X.; Wang, Z.; Zhang, H.; Quan, Z. Pressure-Induced Phase Engineering of Gold Nanostructures. *J. Am. Chem. Soc.* **2018**, *140*, 15783−15790.
(32) Westenfelder, B.; Biskupek, J.; Meyer, J. C.; Kurasch, S.; Lin, X.; Scholz, F.; Gross, A.; Kaiser, U. Bottom-up Formation of Robust Gold Carbide. *Sci. Rep.* **2015**, *5*, 8891.
(33) Barth, J. V.; Brune, H.; Ertl, G.; Behm, R. J. Scanning Tunneling Microscopy Observations on the Reconstructed Au(111) Surface: Atomic Structure, Long-Range Superstructure, Rotational Domains, and Surface Defects. *Phys. Rev. B: Condens. Matter Mater. Phys.* **1990**, *42*, 9307−9318.
(34) Xiao, L.; Tollberg, B.; Hu, X.; Wang, L. Structural Study of Gold Clusters. *J. Chem. Phys.* **2006**, *124*, 114309.
(35) Li, P.; Ding, F. Origin of the Herringbone Reconstruction of Au(111) Surface at the Atomic Scale. *Sci. Adv.* **2022**, *8*, No. eabq2900.
(36) Häkkinen, H. Atomic and Electronic Structure of Gold Clusters: Understanding Flakes, Cages and Superatoms from Simple Concepts. *Chem. Soc. Rev.* **2008**, *37*, 1847−1859.
(37) Li, X. B.; Wang, H. Y.; Yang, X. D.; Zhu, Z. H.; Tang, Y. J. Size Dependence of the Structures and Energetic and Electronic Properties of Gold Clusters. *J. Chem. Phys.* **2007**, *126*, 084505.
(38) Yajadda, M. M. A.; Müller, K. H.; Ostrikov, K. Effect of Coulomb Blockade, Gold Resistance, and Thermal Expansion on the Electrical Resistance of Ultrathin Gold Films. *Phys. Rev. B: Condens. Matter Mater. Phys.* **2011**, *84*, 235431.
(39) Koppen, J. V.; Hapka, M.; Szczęśniak, M. M.; Chałasiński, G. Optical Absorption Spectra of Gold Clusters Au n (n 4, 6, 8,12, 20) from Long-Range Corrected Functionals with Optimal Tuning. *J. Chem. Phys.* **2012**, *137*, 114302.
(40) Lecoultre, S.; Rydlo, A.; Félix, C.; Buttet, J.; Gilb, S.; Harbich, W. UV-Visible Absorption of Small Gold Clusters in Neon: Aun (n 1-5 and 7-9). *J. Chem. Phys.* **2011**, *134*, 074302.

https://doi.org/10.1021/acsami.2c19743
ACS Appl. Mater. Interfaces 2022, 14, 54992−55003